

pubs.acs.org/NanoLett Letter

Improving Oxygen Reduction Performance of Surface-Layer-Controlled Pt—Ni Nano-Octahedra via Gaseous Etching

Can Li, Soonho Kwon, Xiaobo Chen, Lihua Zhang, Anju Sharma, Shaojie Jiang, Hanlei Zhang, Ming Zhou, Jinfong Pan, Guangwen Zhou, William A. Goddard III,* and Jiye Fang*



Cite This: https://doi.org/10.1021/acs.nanolett.3c00567



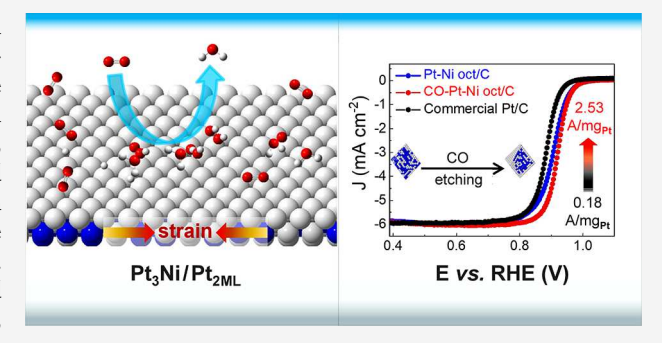
ACCESS I

III Metrics & More

Article Recommendations

s Supporting Information

ABSTRACT: This study demonstrates an atomic composition manipulation on Pt–Ni nano-octahedra to enhance their electrocatalytic performance. By selectively extracting Ni atoms from the {111} facets of the Pt–Ni nano-octahedra using gaseous carbon monoxide at an elevated temperature, a Pt-rich shell is formed, resulting in an ~2 atomic layer Pt-skin. The surface-engineered octahedral nanocatalyst exhibits a significant enhancement in both mass activity (~1.8-fold) and specific activity (~2.2-fold) toward the oxygen reduction reaction compared with its unmodified counterpart. After 20,000 potential cycles of durability tests, the surface-etched Pt–Ni nano-octahedral sample shows a mass activity of 1.50 A/mg_{Pt}, exceeding the initial mass activity of the unetched counterpart (1.40



 A/mg_{Pt}) and outperforming the benchmark Pt/C (0.18 A/mg_{Pt}) by a factor of 8. DFT calculations predict this improvement with the Pt surface layers and support these experimental observations. This surface-engineering protocol provides a promising strategy for developing novel electrocatalysts with improved catalytic features.

KEYWORDS: gaseous etching, oxygen reduction reaction, Pt₃Ni nano-octahedron, Pt-shell {111} facets; deep learning

Platinum (Pt)-based nanocrystals (NCs) constitute a class of most promising actalant (of most promising catalysts for electrochemical reactions in green energy conversion devices, such as the oxygen reduction reaction (ORR) at the cathode of fuel cells. 1-5 To reduce the utilization of the precious Pt element and to enhance the ORR performance, many strategies have been demonstrated, such as alloying a 3d transition metal into the Pt lattice to provide a ligand effect that shifts the Pt d-band center, engineering the NC morphology to control the surface atomic arrangement on the desired facet, and developing a core-shell structure with a Pt-rich surface in the presence of strain effects. 6-17 Among these efforts, it has been reported that Pt₃Ni-based octahedral nanocatalysts containing exclusive {111} facets exhibit promising performance toward the ORR. 18-30 Since it was determined that extended single crystal surfaces of Pt₃Ni(111) exhibited an enhanced ORR activity that is 10-fold higher than Pt(111) and 90-fold higher than the current state-of-the-art Pt/C catalysts, 20 we have developed a wet-chemical synthesis approach in the presence of tungsten carbonyl $[W(CO)_6]$ to successfully "transfer" exclusive and well-preserved {111} facets to the nanophase of Pt₃Ni. 18 The Pt₃Ni nano-octahedra produced from this synthesis strategy show superior ORR activity, demonstrating 64-time enhancement (octahedral Pt_{2.5}Ni/C vs benchmark Pt/ C) after acidic treatment. 19,27 Nevertheless, these Pt–Ni catalysts face a stability challenge due to the potential Ni-

leaching in acidic environments. Various surface engineering efforts, including the doping of a third transition metal (such as Co, ²² Ga, ³¹ Mo, ^{32,33} or Rh²⁴) to the Pt–Ni lattice, have been made to address this issue. We have developed an alternative protocol for dealloying of the Ni-component from PtNi₄ tetrahexahedral (THH) NCs through a carbon monoxide (CO) gaseous etching process in which most of the surface Ni atoms were pre-extracted by CO, being removed *via* producing a Ni(CO)₄ gaseous product at an elevated temperature. This results in Pt₃Ni THH nanoframes with a Pt-rich layer on the outmost layers. ³⁴ After removal of Ni with surface structure control in this novel process, the segregated compressively strained Pt layers on the 3D-nanoframes showed a downshifted *d*-band center, efficiently facilitating electrochemical reactions with demonstrated improved catalytic performance toward the ORR and formic acid oxidation in acidic solutions.

In this study, we applied the CO gaseous etching approach to octahedral Pt₃Ni NCs, one class of the most viable electrocatalysts for the ORR. We anticipated that a Pt-rich

Received: February 13, 2023 Revised: April 5, 2023



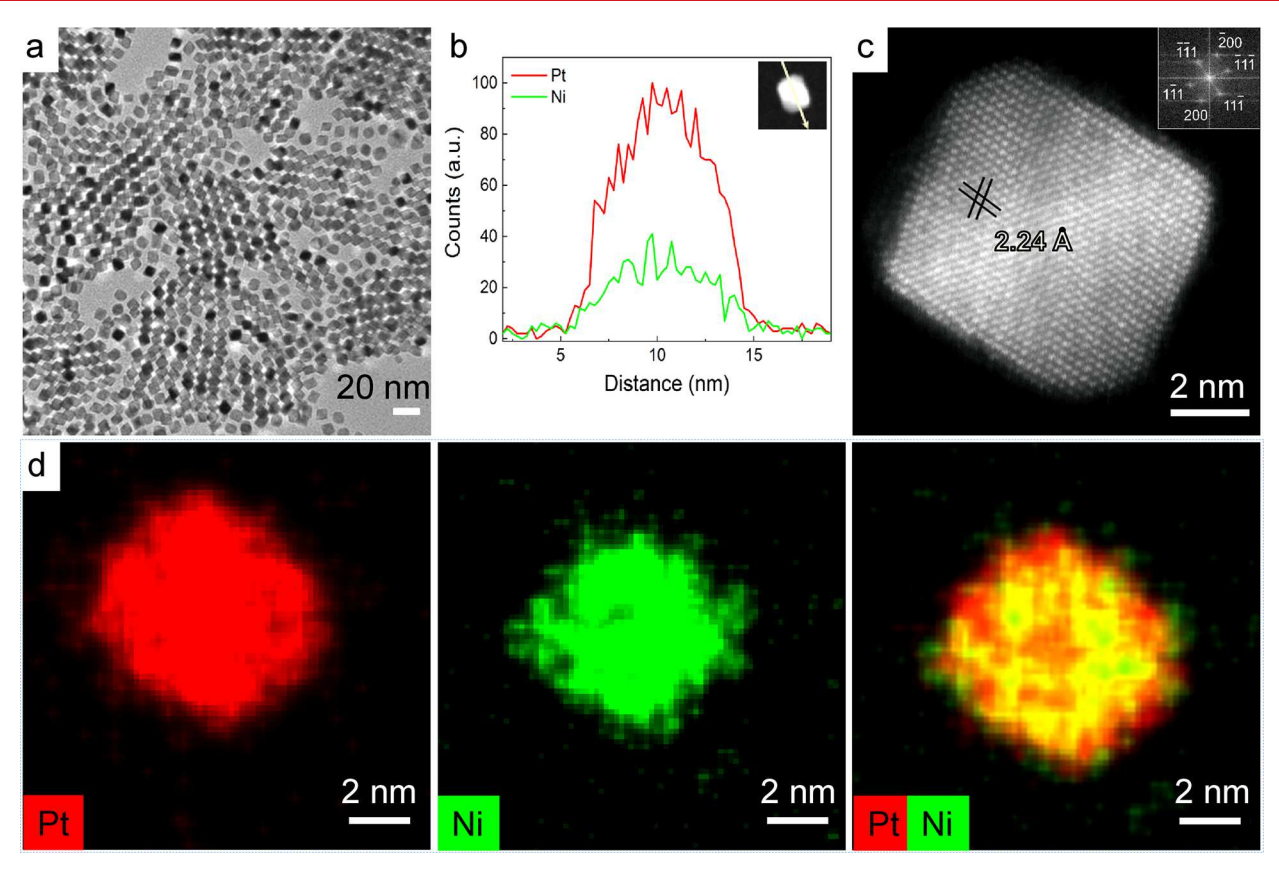


Figure 1. Characterization of the as-synthesized Pt-Ni octahedral NCs. (a) Typical TEM image of the Pt-Ni octahedra. (b) HAADF-STEM EDX line scan profile of an octahedron NC along the arrow-marked direction indicated in the inserted HAADF-STEM image. (c) HAADF-STEM high-resolution image of an octahedron in the zone axis of [110]. The inset in (c) is a diffractogram of the HAADF image. (d) HAADF-STEM EDX elemental maps of a representative octahedron (Pt/red, Ni/green), revealing spatial distributions of Pt and Ni atoms.

atomic shell could be created on the Pt-Ni octahedra with well-preserved Pt₃Ni (111) facets after this surface engineering of Ni dealloying using CO gas, from which improvement in durability and activity toward the ORR was expected. Major steps for preparing the surface-engineered Pt-Ni octahedra/C catalyst are summarized in Scheme 1 in the Supporting Information. Typical high-angle annular dark-field scanning transmission electron microscopic (HAADF-STEM) and transmission electron microscopic (TEM) images of the {111} face-terminated Pt-Ni nano-octahedra with uniform size and shape are shown in Figure S1. These NCs were subsequently loaded onto carbon black and designated as "Pt-Ni oct/C" (Figure S2). Next, a CO-etching process was carried out to manipulate their surface structure, generating surfaceengineered Pt-Ni octahedral electrocatalysts (designated as "CO-Pt-Ni oct/C").

Figure 1a shows a zoom-out TEM view of the as-synthesized monodisperse Pt–Ni nano-octahedra. Their average edge length was determined as 9.5 ± 0.8 nm with a reasonably narrow size distribution based on a direct measurement of ~100 randomly selected [110]-oriented nano-octahedra from an HAADF-STEM image (Figure S3a-c). To consider the NC sampling in all orientations, the average edge length was further refined as 10.4 nm through a deep-learning algorithm (Mask R-CNN model) based on a size input from a 2D HAADF-STEM imaging area containing ~100 nano-octahedra with all of the four-type octahedral projections (Figure S3c-g). Figure 1b is the HAADF-STEM energy dispersive X-ray spectroscopic (EDX) line scan profile of a typical nano-

octahedron for elements Pt (red) and Ni (green) along the arrow direction indicated in the inserted HAADF-STEM image, showing the element fractions in the NC. The HAADF-STEM image (Figure 1c) taken from an individual octahedron along the [011] zone axis exhibits a single-crystal structure with exposed (111) facets. The lattice spacing between the (111) crystallographic planes of the NC was measured as 2.24 A. The inset in Figure 1c shows a diffractogram (fast Fourier transform) of the HAADF image, while the indexed spots correspond to the fcc (111) lattice plane, 20 showing its high crystallinity. The Figure 1d panel illustrates HAADF-STEM EDX elemental maps of a Pt-Ni nano-octahedron (Pt/red, Ni/green). The EDX line scan (Figure 1b) and EDX mapping profiles (Figure 1d) suggest a uniform composition distribution throughout the entire NC, indicating the coreduction of Pt- and Ni-precursors during the synthesis process. As shown in Table S1, the composition of the bulk octahedral Pt-Ni NCs was also determined using an inductively coupled plasmaoptical emission spectrometry (ICP-OES) technique, showing that the Pt/Ni atomic ratio ($R_{Pt/Ni} = 2.57$ or Pt:Ni = 72:28) is consistent with the proportion measured by EDX elemental mapping ($R_{Pt/Ni} = 2.57$ or Pt:Ni = 72:28).

We report here similar analyses on CO-Pt-Ni oct/C. As shown in Figure 2a, the TEM image of the carbon-supported Pt-Ni NCs after the CO-etching indicates that the particles still preserve their octahedral morphology and are mono-dispersed with no aggregation. Figure 2b presents the EDX line-scan profiles of CO-Pt-Ni oct/C for Pt (red) and Ni (green) elements along the arrow direction indicated in the

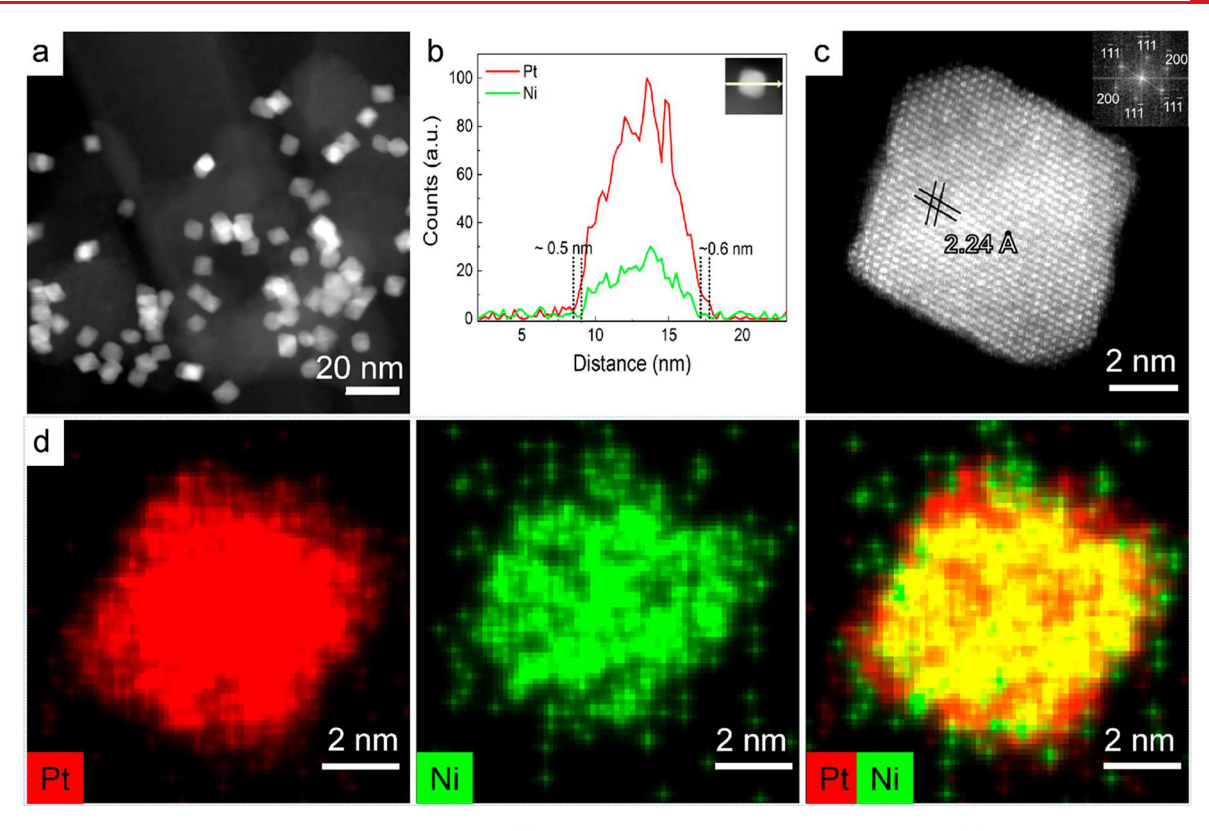


Figure 2. Characterization of the CO-Pt-Ni oct/C catalysts. (a) HAADF-STEM image of CO-Pt-Ni oct/C. (b) HAADF-STEM EDX line scan profile of a CO-Pt-Ni oct/C NC along the arrow direction indicated in the inserted HAADF-STEM image. (c) HAADF-STEM high-resolution image of an octahedron in the zone axis of [110]. The inset in (c) is a diffractogram of the HAADF image. (d) HAADF-STEM EDX elemental maps of a representative octahedron (Pt/red, Ni/green).

inserted HAADF-STEM image, showing a Pt-Ni@Pt core@ shell structure with a thin Pt-shell layer (~0.5 nm, equivalent to ~2 atomic layers). The HAADF-STEM image shown in Figure 2c was taken from a typical individual CO-Pt-Ni oct/C NC along the [011] zone axis, demonstrating that the exposed (111) facets were well-preserved on the surfaces after the COetching treatment, while the lattice spacing between the (111) crystallographic planes of the NC was not changed (2.24 Å). The diffractogram (shown in the inset of Figure 2c) also confirms the fcc structure, which is the same as for the untreated samples. The EDX maps (Figure 2d) show more Pt components in the outer layers of the octahedral NC compared with the Ni distribution, further verifying the core@shell structure generated during the CO-etching treatment. The composition of the CO-Pt-Ni oct/C sample was also analyzed using the ICP-OES technique, where the Pt/Ni atomic ratio was determined as $R_{Pt/Ni}$ = 2.85 (or Pt:Ni = 74:26), which is consistent with the outcome from the EDX elemental mapping ($R_{Pt/Ni} = 2.70$ or Pt:Ni = 73:27). These analysis results clearly suggest that some Ni atoms were effectively removed from the surface of the octahedral Pt-Ni NCs after this CO gaseous etching process.

The phase structures of the aforementioned bulk Pt–Ni NCs were also investigated using powder X-ray diffraction (XRD) technique. As shown in Figure 3a, both octahedral Pt–Ni samples before and after the CO-etching treatment exhibit highly crystalline fcc structures of Pt₃Ni¹⁶ with a right-shift of their diffraction peaks compared with the pure Pt XRD pattern (refer to JCPDS-ICDD card 87-0640) due to the incorporation of Ni atoms into the Pt lattice. Pawley fitting verifies the $Fm\overline{3}m$ symmetry on both Pt–Ni samples and also shows a

slight increase of the unit cell parameter, a, after the COetching treatment (Figure S4), implying the removal of Ni atoms. The reduction of the Ni fraction in CO-Pt-Ni oct/C is further confirmed by the left-shift of its diffraction peaks (e.g., ~0.2 degrees in 2θ at (111) peak, Figure 3b) according to the Pawley fitting, implying extraction of Ni from the Pt-Ni NCs by the CO-etching and the possible presence of a Pt-rich surface on the octahedral NCs after CO-etching treatment.^{3,8} The X-ray photoelectron spectroscopic (XPS) technique was also used to identify possible changes in the electronic structure of the Pt-Ni NCs before and after the CO-etching treatment. The Pt 4f spectrum (Figure 3c) implies the dominance of zerovalent Pt in both the Pt-Ni oct/C and CO-Pt-Ni oct/C catalysts. Compared to the zerovalent Pt in pure Pt metal (71.0 eV), the binding energy of Pt 4f peaks in Pt-Ni oct/C increased by ~0.3 eV. A similar Pt 4f binding energy was also observed in the CO-Pt-Ni oct/C sample. On the other hand, the Ni 2p XPS spectrum of Pt-Ni oct/C (Figure 3d) shows signs of both Ni^o and Ni²⁺, possibly due to the presence of Ni(OH)₂ from the surface oxidation of Ni. However, the Ni²⁺ signal was dramatically suppressed in the XPS spectrum of CO-Pt-Ni oct/C, indicating the absence of Ni²⁺ on the surface of the CO-treated sample. Combined with the TEM information, this result further helps understand the CO gaseous etching. In the reducing atmosphere at an elevated temperature, the oxidized Ni species on the NC surfaces should be reduced to metallic Ni. The zerovalent Ni further reacted with CO to form gaseous Ni(CO)₄ with subsequent removal from the NC surface by the CO stream, eventually generating a Pt(111) thin shell on the NC.34 In addition, we recorded the W 4f spectrum (Figure S5). Unlike previous

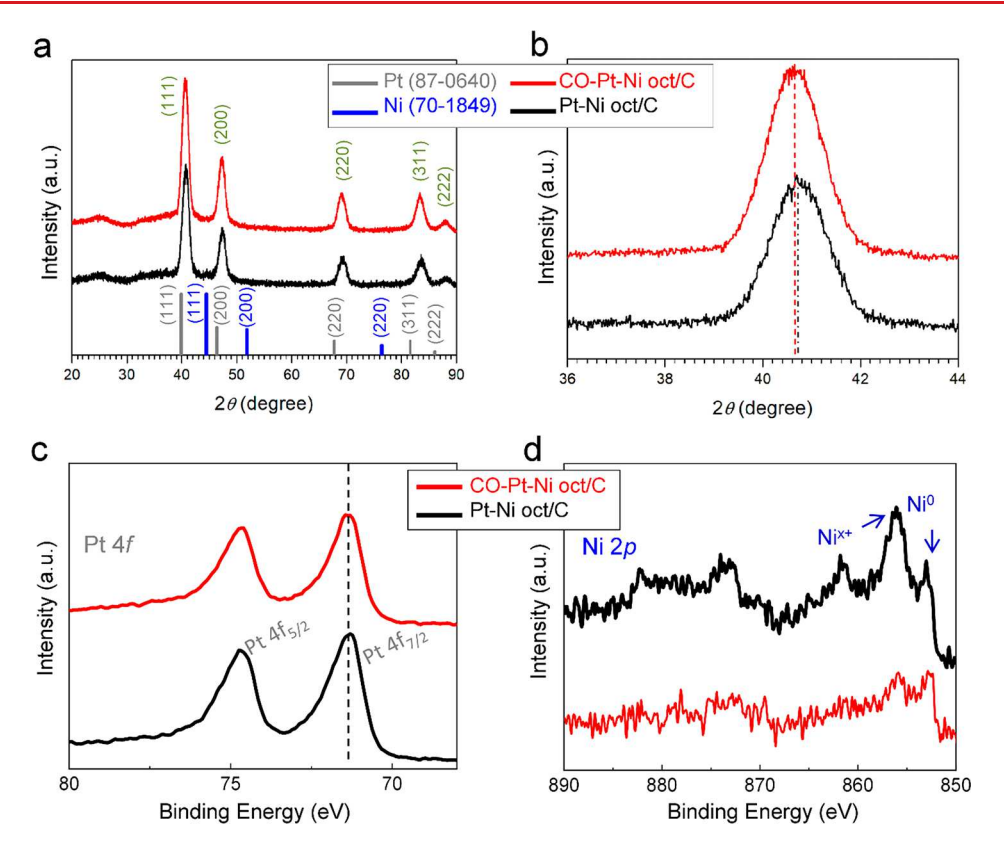


Figure 3. XRD and XPS characterizations of the octahedral Pt–Ni NCs before and after the CO-etching treatment. (a) and (b) XRD patterns of Pt–Ni oct/C (black) and CO-Pt–Ni oct/C (red) in a full-range scan and peak (111) scan, respectively. (c) and (d) XPS spectra of the Pt 4f and Ni 2p, respectively. The gray and blue lines on the bottom of (a) show standard XRD patterns of Pt and Ni (JCPDS-ICDD cards 87-0640 and 70-1849), respectively.

reports in which WOx was detected from the product even though W does not incorporate into the lattice of Pt-Ni or Pt-Fe under the specified synthesis condition, 16,27,35 we did not detect W-species by XPS from both Pt-Ni oct/C and CO-Pt-Ni oct/C samples, indicating the effectiveness of the cleaning process used in this work. It is worth pointing out that the complete removal of W components from the NCs prior to the surface treatment is required to ensure the success of the surface engineering via the gaseous etching and their accurate comparison in terms of the ORR performance. In addition, R_{Pt/Ni} based on the XPS data shows the same trend of composition change before and after this CO-etching process, that is, $R_{Pt/N_i} = 1.44$ (or Pt:Ni = 59:41) vs $R_{Pt/N_i} = 2.13$ (or Pt:Ni = 68:32), respectively. However, these XPS-based Pt/Ni atomic ratios are fairly far from R_{Pt/Ni} determined from ICP-OES and EDX, exhibiting higher Ni fractions (Table S1). This could be due to the inhomogeneous distribution of Pt and Ni over the whole Pt-Ni octahedral NC as a random nanoalloy. During the NC synthesis, the Pt-precursors are easily reduced to Pt atoms for early nucleation ($E_{pt^{2+}/Pt}^{0} = 1.18 \text{ V}$) compared with the Ni-precursors $(E_{Ni^{2+}/Ni}^{o}) = -0.257$ V), leading to abundant Ni-components "segregated" on the upper mantle of the seeds. Unlike ICP and EDX analyses that correspond to the bulk contents, only the surface compositions are sensitive to XPS. This is also consistent with the fact that the XPSdetermined nickel-loss-percentage (~22%) after the CO etching process, defined as (Ni at%_{before process} - Ni at %_{after process})/Ni at%_{before process}, is much higher than those measured by ICP-OES (\sim 7%) and EDX (\sim 4%).

Figure 4a shows the anodic ORR polarization curves of the three samples. CO-Pt-Ni oct/C exhibited a half-wave potential value $(E_{1/2})$ of 0.933 V vs a reversible hydrogen electrode (RHE), which is ~47 mV more positive than that of Pt/C and ~ 12 mV more positive than that of Pt-Ni oct/C. The kinetic current was then calculated based on the Koutecky-Levich equation and normalized against the mass loading of Pt on the electrode or electrochemical active surface area (ECSA) at 0.90 V vs RHE to calculate the mass activity (MA) or specific activity (SA), respectively. As illustrated in Figure 4b, the MA of CO-Pt-Ni oct/C was determined as 2.53 A/mg_{Pt}, which is \sim 1.8 times and \sim 14 times as high as that of Pt–Ni oct/C (1.40 A/mg_{Pt}) and the benchmark Pt/C (0.18 A/mg_{Pt}), respectively. CO-Pt-Ni oct/C also showed superior specific activity, and with an SA (6.02 mA/cm^2) that is ~ 2.2 times and ~23 times as high as that of Pt-Ni oct/C (2.75 mA/cm^2) and the benchmark Pt/C (0.26 mA/cm^2), respectively.

The durability of the CO-Pt-Ni oct/C catalysts was further evaluated through accelerated durability tests (ADTs) by applying continuous potential cycling between 0.60 and 1.0 V νs RHE in the O₂-saturated HClO₄ solution at room temperature. After 20,000 cycles of ADT, we observed a downshift of only ~9 mV (Figure 4c), demonstrating remarkable stability toward the ORR. From the CV profiles (Figure S6) recorded every 10,000 potential cycles, we observed that the peak strength of adsorption and desorption of hydrogen (H_{UPD}) decreased slightly, implying that surface area loss can explain the activity decrease of the as-achieved catalyst. As shown in Figure 4d, the MA of CO-Pt-Ni oct/C

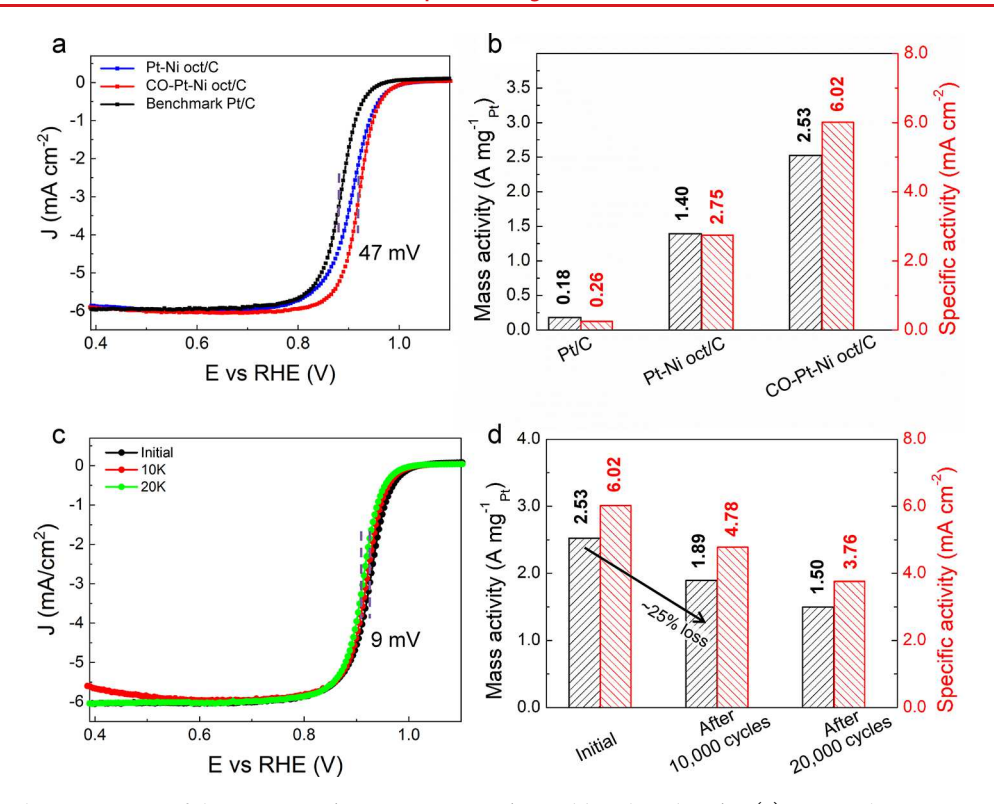


Figure 4. Electrocatalytic properties of the Pt–Ni oct/C, CO-Pt–Ni oct/C, and benchmark Pt/C. (a) ORR polarization curves recorded in O_2 -saturated 0.1 M HClO $_4$ solutions with a potential scan rate of 5 mV/s and an electrode rotation speed of 1,600 rpm. (b) Mass and specific activities at 0.90 V ν s RHE. (c) ORR polarization curves of the CO-Pt–Ni oct/C catalyst before and after durability tests in O_2 -saturated 0.1 M HClO $_4$ at 1,600 rpm and a scan rate of 5 mV/s. (d) Mass and specific activities of the CO-Pt–Ni oct/C catalyst at 0.90 V ν s RHE before and after durability tests.

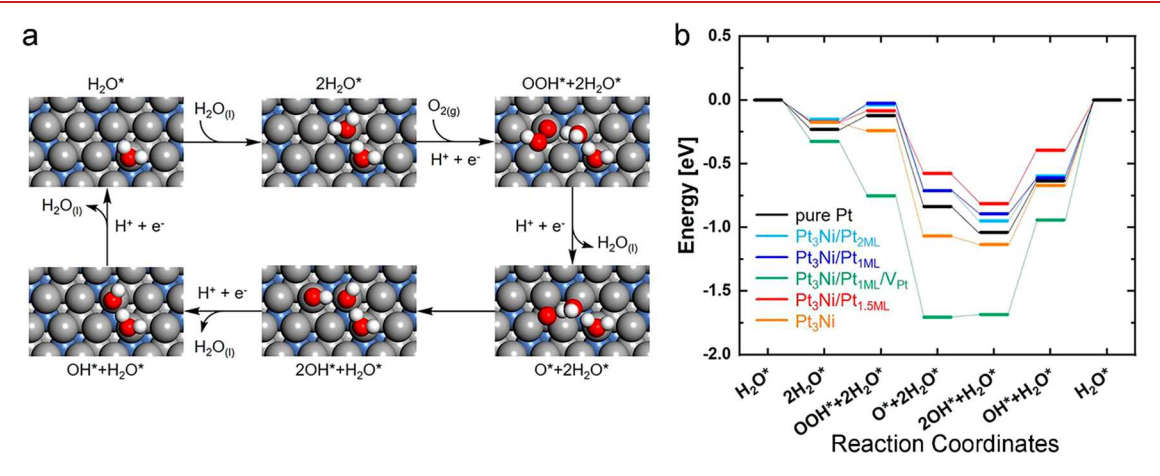


Figure 5. Surface models and the Gibbs free energy diagram of Pt-Ni catalysts for the ORR. (a) The four-electron ORR pathway. The white, red, gray, and blue spheres represent H, O, Pt, and Ni atoms, respectively. (b) Gibbs free energy diagram for the ORR pathway on various Pt-Ni surface models at 1.23 V vs RHE.

dropped to 1.89 A/mg_{Pt} after 10,000 potential cycles and to 1.50 A/mg_{Pt} after 20,000 potential cycles. But this still exceeds the initial mass activities of its unmodified counterpart and the benchmark Pt/C catalysts. Based on the TEM observations and corresponding EDX analysis (Figures S7, S8), the particles of CO-Pt–Ni oct/C became more truncated/spherical after the ADTs. Compared to the morphology before the durability test, the fractional decrease of the Pt–Ni(111) facet should be attributed to the loss of MA. Although the ICP-OES-based (or EDX-based) Pt/Ni molar ratio, $R_{\rm Pt/Ni}$, increased from 2.85 to 3.76 (or from 2.70 to 3.55) after the ADTs (20,000 potential cycles), showing a nickel-loss-percentage (defined above) of

 $\sim\!19\%$ (based on either the ICP-OES or EDX data), it is apparent that more Ni contents are retained in CO-Pt—Ni oct/C by comparing with the corresponding nickel-loss-percentage of the unetched sample (Pt—Ni oct/C, $\sim\!39\%$ from ICP-OES; $\sim\!36\%$ from EDX) based on the data provided in Table S1. The nickel-loss-percentage of CO-Pt—Ni oct/C is also lower than that reported previously. This advantage can be attributed to the more stable Pt₃Ni/Pt₂ ML/V_{Pt} surface structure in the CO-treated catalyst (vide infra).

To understand the correlation between the surface structure and ORR performance, we carried out Quantum Mechanics (QM) calculations (at the PBE-D3 flavor of DFT) using **Nano Letters** pubs.acs.org/NanoLett

various Pt₃Ni(111) surface models to study the effect of different compositions, configurations, and points defects (Figure S9).

- Pt₃Ni/Pt_{1 ML} denotes a monolayer (ML) of pure Pt with a Pt₃Ni substrate,
- Pt₃Ni/Pt_{2 ML} denotes two MLs of pure Pt with a Pt₃Ni substrate,
- Pt₃Ni/Pt_{1.5 ML} represents the model consisting of the top Pt ML with a 1:1 atomic ratio of Ni/Pt in the first sublayer,20
- We also included pure Pt₃Ni and
- Pt₃Ni/Pt_{1 ML}/V_{Pt} which has 0.25 ML of Pt vacancies based on Pt₃Ni/Pt_{1 ML} to mimic our Ni-leaching process.

The four-electron ORR pathway via peroxy intermediates is given by the elementary steps

- (1) $O_{2(g)}+H^++e^-\leftrightarrow OOH^*$: $O_{2(g)}$ reduction (2) $OOH^*+H^++e^-\leftrightarrow O^*$: OOH^* reduction
- (3) $O^* + H_2O_{(1)} \leftrightarrow 2OH^*$: O^* hydrolysis
- (4) $2 \times (OH^* H^+ + e^- \leftrightarrow H_2O_{(1)})$: Water formation

Based on a QM metadynamics study using five layers of explicit solvent, Cheng et al.36 showed that

- at a potential above 0.87 V vs RHE, the rate-determining step (RDS) on Pt(111) is the electrochemical reduction of OH* to form water, step 4,
- at a potential below 0.87 V vs RHE, the RDS is the nonelectrochemical surface oxygen (O*) hydrolysis to produce two OH*, step 3.

The ORR pathway and corresponding free energy diagram at 1.23 V vs RHE are shown in Figure 5a. We found that the overpotential is determined by the OH* reduction (water formation) step 4 without exception. We calculated the overpotential of each (111) surface to be

- 0.63 V for pure Pt,
- 0.59 V for $Pt_3Ni/Pt_{2 ML}$,
- 0.61 V for Pt₃Ni/Pt_{1 ML},
- 0.42 V for $Pt_3Ni/Pt_{1.5 \text{ ML}}$,
- 0.94 V for $(Pt_3Ni/Pt_{1 \text{ ML}}/V_{Pt})$, and
- 0.67 V for pure Pt₃Ni.

Although Pt₃Ni/Pt_{1.5 ML} is the most active phase with the 0.21 V lower overpotential compared to pure Pt, we note that the Pt₃Ni/Pt_{2 ML} model has a 0.04 V lower overpotential than pure Pt which is in line with the ~47 mV higher $E_{1/2}$ for CO– Pt-Ni oct/C compared to Pt/C. Pt₃Ni/Pt_{2 ML} also has 4.62 Åthick pure Pt layers (2 ML), which agrees with our EDX analysis (Figure 2b). This activity enhancement originates from the weaker binding of OH* on Pt, facilitating its reduction to water. The reaction free energy of O* hydrolysis does not depend significantly on the Ni incorporation in the sublayers (Table S2) confirming that the water formation step determines ORR activity. We found that the presence of vacancies (Pt₃Ni/Pt_{1 ML}/V_{Pt}) induces stronger binding of all reaction intermediates leading to a high overpotential of 0.94 V while also making the O hydrolysis step endothermic (Figure 5b). Therefore, based on the high performance of our catalysts, we deduced that the surface of our catalyst is effectively cured to a clean Pt skin during the CO etching. Although the activity could be further enhanced by increasing the Ni ratio up to 50% in the first sublayer, a strong interaction between surface oxygen and oxophilic Ni near the surface and the resulting Ni dissolution would likely perturb the surface Pt during the ORR causing deterioration in performance. We conclude that the

preparation of close-packed Pt 2MLs through CO-etching effectively prevents the Ni-O interaction, leading to the observed high durability for the ORR.

In conclusion, we synthesized Pt-Ni nano-octahedra in an average edge length of ~9.5 nm (The deep-learning algorithm suggests 10.4 nm as the average edge length with a consideration of all four-type octahedral projections.) and demonstrated the atomic manipulation of the surface composition of NCs via the CO gaseous etching process. During the CO-etching treatment at an elevated temperature, the octahedral morphology of Pt-Ni NCs was well preserved with {111} facets, while a Pt-rich shell with ~2 atomic layers was generated through the extraction of Ni atoms. We showed that this unique nanostructure exhibits superior electrocatalytic activity toward the ORR in acid media when compared with the octahedral Pt-Ni counterpart without the Pt-shell and the benchmark Pt/C. We further determined that the CO-treated octahedral Pt-Ni nanocatalysts delayed the decay in the ORR activity that might be caused by Ni leaching/morphology deformation and would occur in their unmodified counterpart and the benchmark Pt/C sooner. Our QM calculations confirmed that the model of two pure Pt monolayers on top of the Pt₃Ni substrate is the most consistent. Thus, this work provides a new platform to improve Pt-Ni-based ORR catalysts. Moreover, this gaseous etching protocol could be extended to other types of electrocatalyst development to further maximize their ORR performance.

ASSOCIATED CONTENT

Supporting Information

The Supporting Information is available free of charge at https://pubs.acs.org/doi/10.1021/acs.nanolett.3c00567.

Experimental method and computation method, schematic illustration of sample preparation procedure, HAADF-STEM and TEM images and size (edge length) determination of the as-prepared octahedral Pt—Ni NCs, TEM image of carbon-supported octahedral Pt-Ni NCs, lattice parameters of CO-Pt-Ni oct/C and Pt-Ni oct/C received from Pawley fitting, CV curves of CO-Pt-Ni oct/C catalysts before and after the accelerated durability tests, EM images and EDX maps/line scan profile of CO-Pt-Ni oct/C after the accelerated durability tests, additional XPS, electrochemical measurements, and DFT results (PDF)

AUTHOR INFORMATION

Corresponding Authors

William A. Goddard III - Materials and Process Simulation Center, California Institute of Technology, Pasadena, California 91125, United States; o orcid.org/0000-0003-0097-5716; Email: wag@caltech.edu

Jive Fang – Department of Chemistry, State University of New York at Binghamton, Binghamton, New York 13902, United States; orcid.org/0000-0003-3703-3204; Email: jfang@ binghamton.edu

Authors

Can Li - Department of Chemistry, State University of New York at Binghamton, Binghamton, New York 13902, United States; orcid.org/0000-0001-8894-5110

- Soonho Kwon Materials and Process Simulation Center, California Institute of Technology, Pasadena, California 91125, United States; orcid.org/0000-0002-9225-3018
- Xiaobo Chen Materials Science and Engineering Program, Department of Mechanical Engineering, State University of New York at Binghamton, Binghamton, New York 13902, United States
- Lihua Zhang Center for Functional Nanomaterials, Brookhaven National Laboratory, Upton, New York 11973, United States
- Anju Sharma Analytical and Diagnostics Lab, State University of New York at Binghamton, Binghamton, New York 13902, United States
- Shaojie Jiang Department of Chemistry, State University of New York at Binghamton, Binghamton, New York 13902, United States; orcid.org/0000-0001-8692-0673
- Hanlei Zhang Advanced Materials Characterization Laboratory, Materials Research Center, Missouri University of Science and Technology, Rolla, Missouri 65409, United States; © orcid.org/0000-0001-6540-0556
- Ming Zhou Department of Chemistry, State University of New York at Binghamton, Binghamton, New York 13902, United States; Occid.org/0000-0002-2708-0501
- Jinfong Pan Department of Chemistry, State University of New York at Binghamton, Binghamton, New York 13902, United States
- Guangwen Zhou Materials Science and Engineering Program, Department of Mechanical Engineering, State University of New York at Binghamton, Binghamton, New York 13902, United States; orcid.org/0000-0002-9243-293X

Complete contact information is available at: https://pubs.acs.org/10.1021/acs.nanolett.3c00567

Author Contributions

C.L., S.K., and X.C. contributed equally to this work.

Notes

The authors declare no competing financial interest.

ACKNOWLEDGMENTS

This work was primarily supported by the National Science Foundation (NSF) under grant DMR-1808383. The theoretical work used the Extreme Science and Engineering Discovery Environment (XSEDE) for DFT calculations, which is supported by the NSF under grant ACI-1548562. W.A.G. is thankful for support by the NSF (CBET-2005250, program manager: Bob McCabe), S.K. acknowledges support from the Resnick Sustainability Institute at Caltech; X.C. and G.Z. are thankful for the financial support by the NSF under grant DMR-1905422. L.Z. acknowledges the use of TEM facilities for the structural characterizations, at the Center for Functional Nanomaterials, which is a U.S. Department of Energy Office of Science User Facility, at Brookhaven National Laboratory under Contract No. DE-SC0012704. Partial lowmagnification TEM imaging work was supported by S3IP/ ADL, the State University of New York at Binghamton.

REFERENCES

(1) Zhou, M.; Li, C.; Fang, J. Noble-Metal Based Random Alloy and Intermetallic Nanocrystals: Syntheses and Applications. *Chem. Rev.* **2021**, *121* (2), 736–795.

- (2) Shi, Y.; Lyu, Z.; Zhao, M.; Chen, R.; Nguyen, Q. N.; Xia, Y. Noble-Metal Nanocrystals with Controlled Shapes for Catalytic and Electrocatalytic Applications. *Chem. Rev.* **2021**, *121* (2), 649–735.
- (3) Li, C.; Yan, S.; Fang, J. Construction of Lattice Strain in Bimetallic Nanostructures and Its Effectiveness in Electrochemical Applications. *Small* **2021**, *17* (46), 2102244.
- (4) Gilroy, K. D.; Ruditskiy, A.; Peng, H. C.; Qin, D.; Xia, Y. Bimetallic Nanocrystals: Syntheses, Properties, and Applications. *Chem. Rev.* **2016**, *116* (18), 10414–10472.
- (5) Stamenkovic, V. R.; Strmcnik, D.; Lopes, P. P.; Markovic, N. M. Energy and Fuels from Electrochemical Interfaces. *Nat. Mater.* **2017**, *16* (1), 57–69.
- (6) Li, C.; Chen, X.; Zhang, L.; Yan, S.; Sharma, A.; Zhao, B.; Kumbhar, A.; Zhou, G.; Fang, J. Synthesis of Core@Shell Cu-Ni@Pt-Cu Nano-Octahedra and Their Improved MOR Activity. *Angew. Chem., Int. Ed.* **2021**, *60* (14), 7675–7680.
- (7) Zhu, Y.; Peng, J.; Zhu, X.; Bu, L.; Shao, Q.; Pao, C. W.; Hu, Z.; Li, Y.; Wu, J.; Huang, X. A Large-Scalable, Surfactant-Free, and Ultrastable Ru-Doped Pt₃Co Oxygen Reduction Catalyst. *Nano Lett.* **2021**, *21* (15), 6625–6632.
- (8) Xie, M.; Lyu, Z.; Chen, R.; Shen, M.; Cao, Z.; Xia, Y. Pt-Co@Pt Octahedral Nanocrystals: Enhancing Their Activity and Durability toward Oxygen Reduction with an Intermetallic Core and an Ultrathin Shell. J. Am. Chem. Soc. 2021, 143 (22), 8509–8518.
- (9) Xiao, W.; Lei, W.; Gong, M.; Xin, H. L.; Wang, D. Recent Advances of Structurally Ordered Intermetallic Nanoparticles for Electrocatalysis. *ACS Catal.* **2018**, 8 (4), 3237–3256.
- (10) Zhao, X. R.; Xi, C.; Zhang, R.; Song, L.; Wang, C. Y.; Spendelow, J. S.; Frenkel, A. I.; Yang, J.; Xin, H. L.; Sasaki, K. High-Performance Nitrogen-Doped Intermetallic PtNi Catalyst for the Oxygen Reduction Reaction. ACS Catal. 2020, 10 (18), 10637—10645.
- (11) Kim, C.; Dionigi, F.; Beermann, V.; Wang, X.; Möller, T.; Strasser, P. Alloy Nanocatalysts for the Electrochemical Oxygen Reduction (ORR) and the Direct Electrochemical Carbon Dioxide Reduction Reaction (CO₂RR). *Adv. Mater.* **2019**, *31* (31), 1805617. (12) Li, J.; Xi, Z.; Pan, Y. T.; Spendelow, J. S.; Duchesne, P. N.; Su,
- (12) Li, J.; Xi, Z.; Pan, Y. 1.; Spendelow, J. S.; Duchesne, P. N.; Su, D.; Li, Q.; Yu, C.; Yin, Z.; Shen, B.; Kim, Y. S.; Zhang, P.; Sun, S. Fe Stabilization by Intermetallic L1₀-FePt and Pt Catalysis Enhancement in L1₀-FePt/Pt Nanoparticles for Efficient Oxygen Reduction Reaction in Fuel Cells. *J. Am. Chem. Soc.* **2018**, *140* (8), 2926–2932.
- (13) Xiong, Y.; Xiao, L.; Yang, Y.; DiSalvo, F. J.; Abruña, H. D. High-Loading Intermetallic Pt₃Co/C Core—Shell Nanoparticles as Enhanced Activity Electrocatalysts toward the Oxygen Reduction Reaction (ORR). *Chem. Mater.* **2018**, *30* (5), 1532–1539.
- (14) Wang, C.; Lin, C.; Zhang, L.; Quan, Z.; Sun, K.; Zhao, B.; Wang, F.; Porter, N.; Wang, Y.; Fang, J. Pt₃Co Concave Nanocubes: Synthesis, Formation Understanding, and Enhanced Catalytic Activity toward Hydrogenation of Styrene. *Chem. Eur. J.* **2014**, *20* (6), 1753–1759
- (15) Strasser, P.; Koh, S.; Anniyev, T.; Greeley, J.; More, K.; Yu, C.; Liu, Z.; Kaya, S.; Nordlund, D.; Ogasawara, H.; Toney, M. F.; Nilsson, A. Lattice-Strain Control of the Activity in Dealloyed Core—Shell Fuel Cell Catalysts. *Nat. Chem.* **2010**, *2*, 454.
- (16) Zhang, J.; Fang, J. A General Strategy for Preparation of Pt 3d-Transition Metal (Co, Fe, Ni) Nanocubes. *J. Am. Chem. Soc.* **2009**, 131 (51), 18543–18547.
- (17) Stamenkovic, V. R.; Mun, B. S.; Arenz, M.; Mayrhofer, K. J.; Lucas, C. A.; Wang, G.; Ross, P. N.; Markovic, N. M. Trends in Electrocatalysis on Extended and Nanoscale Pt-Bimetallic Alloy Surfaces. *Nat. Mater.* **2007**, *6* (3), 241–247.
- (18) Zhang, J.; Yang, H.; Fang, J.; Zou, S. Synthesis and Oxygen Reduction Activity of Shape-Controlled Pt₃Ni Nanopolyhedra. *Nano Lett.* **2010**, *10* (2), 638–644.
- (19) Choi, S.-I.; Xie, S.; Shao, M.; Odell, J. H.; Lu, N.; Peng, H.-C.; Protsailo, L.; Guerrero, S.; Park, J.; Xia, X.; Wang, J.; Kim, M. J.; Xia, Y. Synthesis and Characterization of 9 nm Pt—Ni Octahedra with a Record High Activity of 3.3 A/mg_{Pt} for the Oxygen Reduction Reaction. *Nano Lett.* **2013**, *13* (7), 3420–3425.

- (20) Stamenkovic, V. R.; Fowler, B.; Mun, B. S.; Wang, G.; Ross, P. N.; Lucas, C. A.; Markovic, N. M. Improved Oxygen Reduction Activity on Pt₃Ni(111) via Increased Surface Site Availability. *Science* **2007**, *315* (5811), 493–497.
- (21) Chen, C.; Kang, Y.; Huo, Z.; Zhu, Z.; Huang, W.; Xin, H. L.; Snyder, J. D.; Li, D.; Herron, J. A.; Mavrikakis, M.; Chi, M.; More, K. L.; Li, Y.; Markovic, N. M.; Somorjai, G. A.; Yang, P.; Stamenkovic, V. R. Highly Crystalline Multimetallic Nanoframes with Three-Dimensional Electrocatalytic Surfaces. *Science* **2014**, *343* (6177), 1339–1343.
- (22) Huang, X. Q.; Zhao, Z. P.; Chen, Y.; Zhu, E. B.; Li, M. F.; Duan, X. F.; Huang, Y. A Rational Design of Carbon-Supported Dispersive Pt-Based Octahedra as Efficient Oxygen Reduction Reaction Catalysts. *Energy Environ. Sci.* **2014**, 7 (9), 2957–2962.
- (23) Huang, X.; Zhao, Z.; Cao, L.; Chen, Y.; Zhu, E.; Lin, Z.; Li, M.; Yan, A.; Zettl, A.; Wang, Y. M.; Duan, X.; Mueller, T.; Huang, Y. High-Performance Transition Metal-Doped Pt₃Ni Octahedra for Oxygen Reduction Reaction. *Science* 2015, 348 (6240), 1230–1234.
- (24) Beermann, V.; Gocyla, M.; Willinger, E.; Rudi, S.; Heggen, M.; Dunin-Borkowski, R. E.; Willinger, M. G.; Strasser, P. Rh-Doped Pt-Ni Octahedral Nanoparticles: Understanding the Correlation between Elemental Distribution, Oxygen Reduction Reaction, and Shape Stability. *Nano Lett.* **2016**, *16* (3), 1719–1725.
- (25) Kong, F.; Ren, Z.; Norouzi Banis, M.; Du, L.; Zhou, X.; Chen, G.; Zhang, L.; Li, J.; Wang, S.; Li, M.; Doyle-Davis, K.; Ma, Y.; Li, R.; Young, A.; Yang, L.; Markiewicz, M.; Tong, Y.; Yin, G.; Du, C.; Luo, J.; Sun, X. Active and Stable Pt–Ni Alloy Octahedra Catalyst for Oxygen Reduction via Near-Surface Atomical Engineering. *ACS Catal.* **2020**, *10* (7), 4205–4214.
- (26) Xiao, F.; Qin, X.; Xu, M.; Zhu, S.; Zhang, L.; Hong, Y.; Choi, S.-I.; Chang, Q.; Xu, Y.; Pan, X.; Shao, M. Impact of Heat Treatment on the Electrochemical Properties of Carbon-Supported Octahedral Pt–Ni Nanoparticles. *ACS Catal.* **2019**, *9* (12), 11189–11198.
- (27) Niu, G.; Zhou, M.; Yang, X.; Park, J.; Lu, N.; Wang, J.; Kim, M. J.; Wang, L.; Xia, Y. Synthesis of Pt-Ni Octahedra in Continuous-Flow Droplet Reactors for the Scalable Production of Highly Active Catalysts toward Oxygen Reduction. *Nano Lett.* **2016**, *16* (6), 3850–3857
- (28) Wu, Y.; Cai, S.; Wang, D.; He, W.; Li, Y. Syntheses of Water-Soluble Octahedral, Truncated Octahedral, and Cubic Pt-Ni Nanocrystals and Their Structure-Activity Study in Model Hydrogenation Reactions. *J. Am. Chem. Soc.* **2012**, *134* (21), 8975–8981.
- (29) Gan, L.; Cui, C.; Heggen, M.; Dionigi, F.; Rudi, S.; Strasser, P. Element-Specific Anisotropic Growth of Shaped Platinum Alloy Nanocrystals. *Science* **2014**, 346 (6216), 1502–1506.
- (30) Becknell, N.; Son, Y.; Kim, D.; Li, D.; Yu, Y.; Niu, Z.; Lei, T.; Sneed, B. T.; More, K. L.; Markovic, N. M.; Stamenkovic, V. R.; Yang, P. Control of Architecture in Rhombic Dodecahedral Pt-Ni Nanoframe Electrocatalysts. *J. Am. Chem. Soc.* **2017**, *139* (34), 11678–11681.
- (31) Lim, J.; Shin, H.; Kim, M.; Lee, H.; Lee, K. S.; Kwon, Y.; Song, D.; Oh, S.; Kim, H.; Cho, E. Ga-Doped Pt-Ni Octahedral Nanoparticles as a Highly Active and Durable Electrocatalyst for Oxygen Reduction Reaction. *Nano Lett.* **2018**, *18* (4), 2450–2458.
- (32) Dionigi, F.; Weber, C. C.; Primbs, M.; Gocyla, M.; Bonastre, A. M.; Spori, C.; Schmies, H.; Hornberger, E.; Kuhl, S.; Drnec, J.; Heggen, M.; Sharman, J.; Dunin-Borkowski, R. E.; Strasser, P. Controlling Near-Surface Ni Composition in Octahedral PtNi(Mo) Nanoparticles by Mo Doping for a Highly Active Oxygen Reduction Reaction Catalyst. *Nano Lett.* **2019**, *19* (10), 6876–6885.
- (33) Jia, Q.; Zhao, Z.; Cao, L.; Li, J.; Ghoshal, S.; Davies, V.; Stavitski, E.; Attenkofer, K.; Liu, Z.; Li, M.; Duan, X.; Mukerjee, S.; Mueller, T.; Huang, Y. Roles of Mo Surface Dopants in Enhancing the ORR Performance of Octahedral PtNi Nanoparticles. *Nano Lett.* **2018**, *18* (2), 798–804.
- (34) Wang, C.; Zhang, L.; Yang, H.; Pan, J.; Liu, J.; Dotse, C.; Luan, Y.; Gao, R.; Lin, C.; Zhang, J.; Kilcrease, J. P.; Wen, X.; Zou, S.; Fang, J. High-Indexed Pt₃Ni Alloy Tetrahexahedral Nanoframes Evolved

- through Preferential CO Etching. Nano Lett. 2017, 17 (4), 2204-
- (35) Wang, C.; Lin, C.; Zhao, B.; Zhang, L.; Kumbhar, A.; Fan, G.; Sun, K.; Zhang, J.; Chen, S.; Fang, J. High-Indexed Pt₃Fe Nanocatalysts and Their Enhanced Catalytic Performance in Dual Organic Reactions. *ChemNanoMat* **2015**, *1* (5), 331–337.
- (36) Cheng, T.; Goddard, W. A.; An, Q.; Xiao, H.; Merinov, B.; Morozov, S. Mechanism and Kinetics of the Electrocatalytic Reaction Responsible for the High Cost of Hydrogen Fuel Cells. *Phys. Chem. Chem. Phys.* **2017**, *19* (4), 2666–2673.